Probing interspatial magnetic flux distributions in ferromagnetic stripe arrays by specular and off-specular polarized neutron scattering

D. Gorkov [1,2,*] B. P. Toperverg [2,3] and H. Zabel [2]

[1] *II. Physikalisches Institut, Universität zu Köln, 50937 Köln, Germany*

[2] *Festkörperphysik/Experimentalphysik, Ruhr-Universität Bochum, 44780 Bochum, Germany*

[3] *Petersburg Nuclear Physics Institute, 188300 Gatchina, Russia*

(Received 11 November 2019; accepted 13 May 2020; published 2 June 2020)

Edge roughness in magnetic stripe arrays is an important structural parameter with a sizable impact on magnetic domains, domain correlation, pinning and propagation of domain walls in micro- and nanostripes proposed for data storage and logic devices. We have investigated two different stripe arrays fabricated by lithographic methods from permalloy $Fe_{22}Ni_{78}$, one with rough edges and another one with smooth edges. Performing polarized neutron reflectivity and polarized neutron off-specular scattering both patterns yield specular reflectivity curves with pronounced Kiessig fringes and well resolved Bragg bands in the off-specular regime due to the lateral periodicity. When applying a saturating magnetic field perpendicular to the stripes, a significant diffuse scattering can be detected close to the total reflection edge where it is enhanced by the Yoneda effect. This diffuse magnetic scattering can be attributed to inhomogeneities of the magnetic induction in the empty space between the stripes. In contrast, the sample with much less edge roughness does not exhibit off-specular diffuse scattering. Thus polarized neutron scattering from stripe patterns is a suitable tool for quantitative characterization of inhomogeneous magnetic flux distribution in the interspace between magnetic stripes invoked by their edge roughness.

DOI: 10.1103/PhysRevB.101.224404

I. INTRODUCTION

Magnetic stripes or wires having a width on the micro- to nanometer length scale are important objects of research and development in the field of magnonics, magnetoelectronics, and spintronics. Nanowires with different aspect ratios confine magnetism to one dimension, providing a laboratory for investigations of magnetization reversal processes [1–5] for controlling domain walls and determining domain wall velocities [6–9], for trapping skyrmions [10–17] and for realization of various domain ground states [18–21]. Furthermore, nanowires have been considered as building elements for three-dimensional magnetic storage devices [14,22,23] and for logic elements [24,25].

As the size of the nanowires decreases, the fabrication of these wires with smooth edges becomes increasingly challenging. Edge roughness affects all characteristic magnetic properties of wires, including hysteresis and domain wall kinetics because of the trapping potential caused by edge roughness [26–32]. Moreover, in arrays of nanowires edge roughness opens up a channel for interaction between the wires via stray magnetic flux emanating from rough edges.

From a structural point of view, edge roughness can be characterized by a number of imaging techniques. However, determining quantitatively the magnetic flux between wires is more challenging. Hall probes are not sufficiently small and magnetic tips of magnetic force microscopes may not be sensitive enough to low density flux. In this work, we show that polarized neutron scattering (PNS) techniques, combining specular polarized neutron reflectivity (PNR), Bragg diffraction as well as diffuse off-specular scattering (OSS), is a suitable method for characterizing the flux density in magnetic nanostripe arrays and in the interspace between the stripes. This sensitivity is due to the fact that polarized neutrons, in contrast to x rays, probe the magnetic flux density (magnetic induction) rather than local magnetic moment distributions. Arrays of magnetic nanowires have been studied in the past extensively by PNR and OSS [33–41], reviews are provided in Refs. [42–44]. However, so far the focus has not been on the interstripe flux density.

This contribution is organized as follows. In Sec. II, we provide some theoretical background on flux distributions in magnetic stripe arrays. In Sec. III, we describe the sample preparation and provide results of structural and magnetic characterizations of two periodic stripe arrays, investigated in more detail via neutron scattering. Before presenting the neutron results in Sec. V, we first discuss the scattering geometry and orientation of the neutron coherence volume with respect to the stripe array in Sec. IV. The results are discussed and summarized in Sec. VI. Some of the more detailed theoretical discussions can be found in Appendices A and B.

II. GENERAL REMARKS ON FLUX LINE DISTRIBUTION IN MAGNETIC STRIPE ARRAYS

We start with the simplest case of an array of narrow soft-magnetic stripes with smooth edges subjected to a

*Dmitry.Gorkov@frm2.tum.de

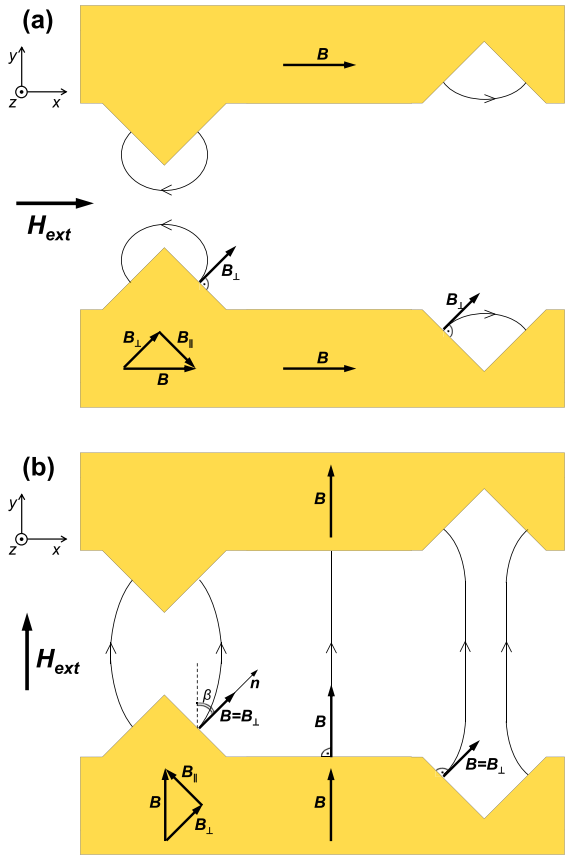

FIG. 1. Scheme of flux line distortions between two stripes with notches at their edges. Saturating field applied (a) parallel and (b) perpendicular to stripes.

homogeneous magnetic field applied parallel to the long axis of the stripes. Due to shape-induced uniaxial anisotropy the stripes with ideally smooth and straight edges are homogeneously magnetized parallel to their long side up to saturation already in relatively weak external field H. As a result, the magnetic induction within the stripes is $B = H + 4\pi M_{\rm sat} \approx 4\pi M_{\rm sat}$, but in the interstripe space $B = H \ll 4\pi M_{\rm sat}$. Magnetic moments in neighboring stripes do not interact with each other, except of those effectively interacting via dipolar fields at their free tips at the sample boundary.

This scenario may not hold for real stripes with rough edges, as schematically illustrated in Fig. 1(a). Here the edge roughness is modeled by a set of notches with flat edge surfaces, but tilted with respect to the stripe axes. Then the magnetic flux may not propagate only within stripes of high magnetic permeability, but also partially percolate into the interstripe space (ISS) affecting the magnetization distribution of neighboring stripes wherever the internal field homogeneity is sufficiently perturbed by the roughness. As a result, edge roughness may generate interaction between adjacent structural elements via stray fields. These fields are rather strong close to the stripe surface and randomly distributed within the range scaled to the edge roughness, but rapidly decays with increasing distance from the stripe edges. If the interstripe separation is much larger than the edge root-mean-square (rms) roughness, then the stray field flux lines are closed. Exiting flux lines from an edge of a stripe preferably return back to the same stripe. However, as the interstripe distance decreases, some flux lines will reach a neighboring stripe, providing a mechanism for interstripe interaction. This may substantially modify the global magnetic properties of the whole pattern, such as shape-induced anisotropy, coercive field, and magnetic hyperdomain formation spanning across several stripes [38,39,41].

A totally different situation takes place for thin stripe arrays saturated in the direction perpendicular to the stripes, as sketched in Fig. 1(b). Let us assume that the stripes are oriented along the x axis, the saturating field is applied along the y axis, while the z axis is perpendicular to the surface of the stripe array. As the component of the magnetic induction vector normal to the boundary between two media is conserved, the magnetic flux lines of a perpendicularly magnetized stripe in the array are not terminated at the stripe edge but penetrate into the ISS, and propagate there until entering into the neighboring stripe.

In case of ideally smooth stripe edges the flux lines between long stripes with high aspect ratio run along the y axis exactly perpendicular to the stripe over about the total stripe thickness and the magnitude of the interstripe induction is nearly equal to that within the stripes. Only in the space close to stripe surfaces, the direction of the flux lines slightly deviates from the y direction and a gradient of the field along the z axis appears, which, in turn, is due to the conservation of the density of the magnetic flux lines and results in a gradient in the y direction. Hence, in case of ideal edges, the configuration of the magnetic induction in the ISS has a flattened barrel like shape and gradients in the x direction are absent.

However, in presence of lateral edge roughness, this field configuration may be severely distorted, giving rise to enhanced inhomogeneities and appreciable gradients due to the stray fields in x, y, and z directions close to the stripe edges. This is schematically illustrated in Fig. 1(b), where edge roughness is imitated, as above, by a set of notches with flat edge surfaces which are tilted with respect to the stripe induction. Then only the normal to notch side component $B_\perp = H_\perp + 4\pi M_\perp$ of the induction vector $\boldsymbol{B}$ and the tangential component $\boldsymbol{H}_\parallel$ of magnetic field vector $\boldsymbol{H}$ are continues, determining the angle and the magnitude of induction in the vicinity of the notch edge surface. Moving away from the edge, the gradients along the x and y axes decrease and on distances much larger than the size of the notches the magnetic flux lines become straighten out.

We will show later that the proper PNR geometry provides quantitative information on the magnetic induction distribution over the stripe pattern with and without edge roughness. In particular, it will be shown that from PNR data one can deduce the mean value of interstripe induction and mean squared deviations of its components tangential to the stripes edges. The results are reported for two orientations of external fields directed along with and perpendicular to stripes for two samples: one with pronounced roughness and the other one with low edge roughness.

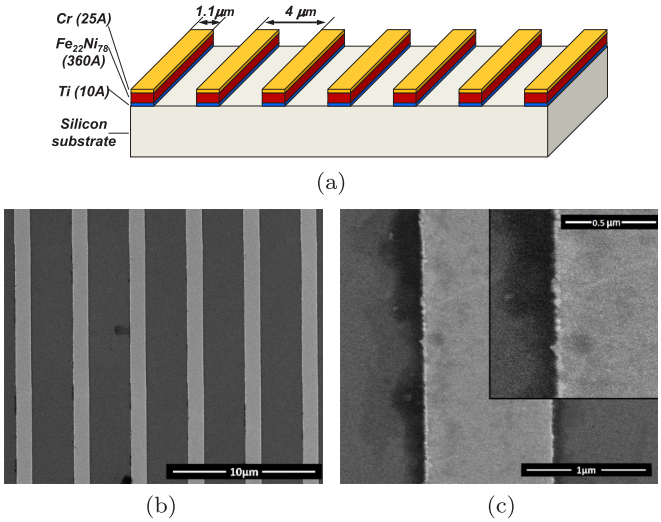

FIG. 2. (a) Scheme of the S1 sample stack with nominal thicknesses of layers. (b) SEM images of the S1 stripe array. Dark-grey color corresponds to the Si substrate. (c) Zoomed SEM image revealing pronounced lateral edge roughness and notches. The inset in the upper right corner shows an enlargement of the edge roughness.

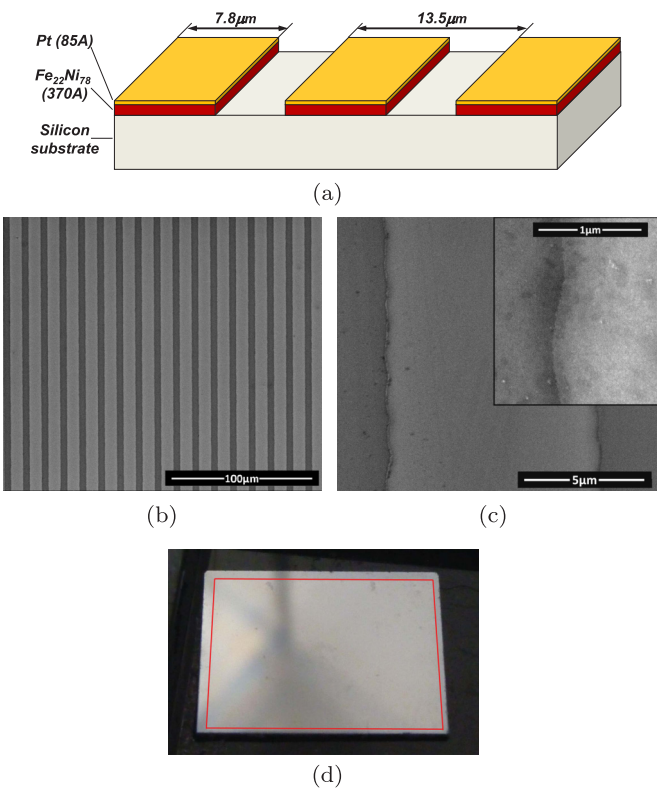

FIG. 3. (a) Scheme of the permalloy stripe array S2 with nominal thicknesses of layers. (b) Overview SEM image of the S2 sample. Dark-gray color corresponds to the Si substrate. (c) Zoomed SEM images showing waviness of the stripe edges with absence of notches. The inset in the upper right corner shows a further enlargement of the wavy edge. (d) Photographic image of the complete sample. Red line shows the boundary of the pattern.

III. SAMPLE PREPARATION, STRUCTURAL CHARACTERIZATION, AND MAGNETIC CHARACTERIZATION

In the following, we discuss sample preparation, structural and magnetic characterization of two samples with different stripe patterns and edge roughnesses labeled S1 and S2.

A. Microstripe array S1

The sample S1 with the size of 20×20 mm^2 consists of an array of parallel permalloy (Py) $Fe_{22}Ni_{78}$ microstripes deposited on a single-crystalline Si(100) substrate with the period $d \approx 4$ μm. Each individual stripe of the S1 sample has a nominal width of $w = 1.1$ μm.

The sample was prepared by a bottom-up lithographic procedure: a cleaned Si substrate was spin-coated with a positive photoresist (Microposit SP2510). Then the resist was baked for 20 min at 100 °C and sequentially exposed to 405-nm laser light using a laser pattern generator. After developing, the remaining pattern was coated with a triple stack of metal films in a sputtering machine at a base pressure of 0.85×10^{-5} mbar and with a sputtering rate of 0.5 Å/s for all layers. First a 10-Å-thick titanium seed layer was sputtered on the silicon wafer, followed by a 360-Å-thick permalloy film, capped by a 25-Å-thick chromium layer for oxidation protection. A final lift-off and cleaning step completed the sample preparation. The layer sequence of the sample stack S1 is sketched in Fig. 2(a). The quality of the final pattern was inspected by scanning electron microscopy imaging (SEM) as presented in Figs. 2(b) and 2(c), confirming the periodicity of the microstripe pattern with pronounced edge roughness.

B. Microstripe array S2

The sample S2 with the size of 8×12 mm^2 consists of an array of parallel permalloy microstripes with a nominal width of $w = 7.8$ μm and lateral period of $d = 13.5$ μm. The stripes were fabricated on a single-crystalline Si(100) substrate and oriented parallel to the longer edge of the sample. In contrast to the sample S1, the sample S2 was prepared by a top-down lithography procedure using a Cr photomask containing the pattern design. The photomask was fixed in a mask aligner and brought in contact with the substrate covered by baked photoresist. Then the photoresist was exposed to 365-nm UV radiation for 40 s through the mask. After exposure and development of the photoresist, the sample stack was sputtered using an Ar ion-beam sputtering machine at a base pressure of better than 5×10^{-9} mbar. For ensuring a homogeneous thickness of the sample, the substrate was rotated during the sputtering process. The deposition rates of the materials were fixed at 0.54 Å/s and 0.63 Å/s for Py and Cr capping layer, respectively. The final sample stack consists of a nominally 370-Å-thick ferromagnetic Py layer directly on the Si substrate without seeding layer, capped by a 85-Å-thick protecting Pt film. The sample design is sketched in Fig. 3(a). SEM images of sample S2 are presented in Figs. 3(b) and 3(c), revealing some smooth waviness of the stripe edges but absence of pronounced sharp notches on the submicrometer scale.

It should be noted that due to the UV lithography procedure using a photomask only the center part of the sample S2 is

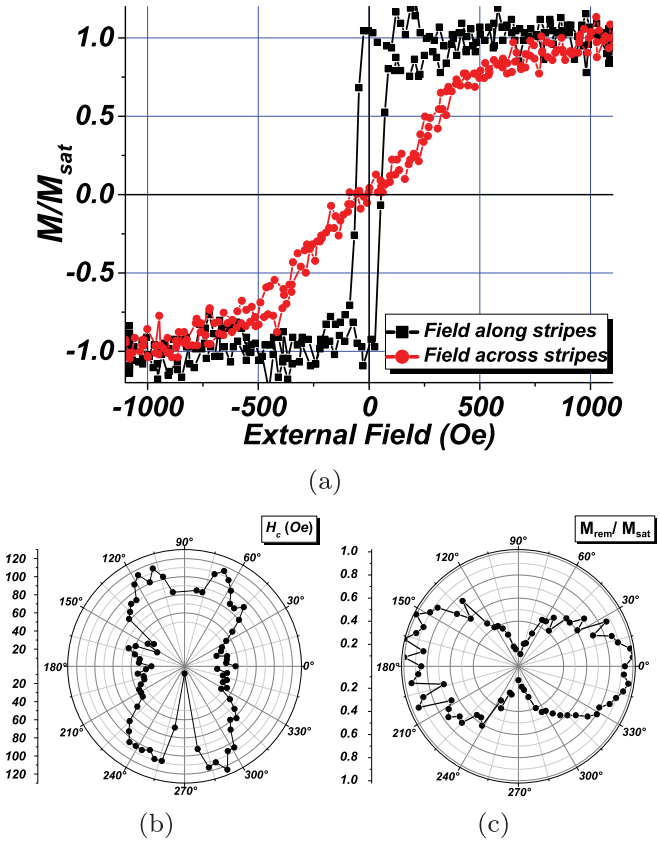

FIG. 4. Magnetic characterization of the sample S1 by L-MOKE-measurements. Zero angle corresponds to stripes oriented parallel to the scattering plane. (a) Hysteresis loops measured with field oriented along and perpendicular to the stripes. (b) Polar plot of coercivity H_c. (c) Polar plot of normalized remanent magnetization $M_{\rm rem}/M_{\rm sat}$.

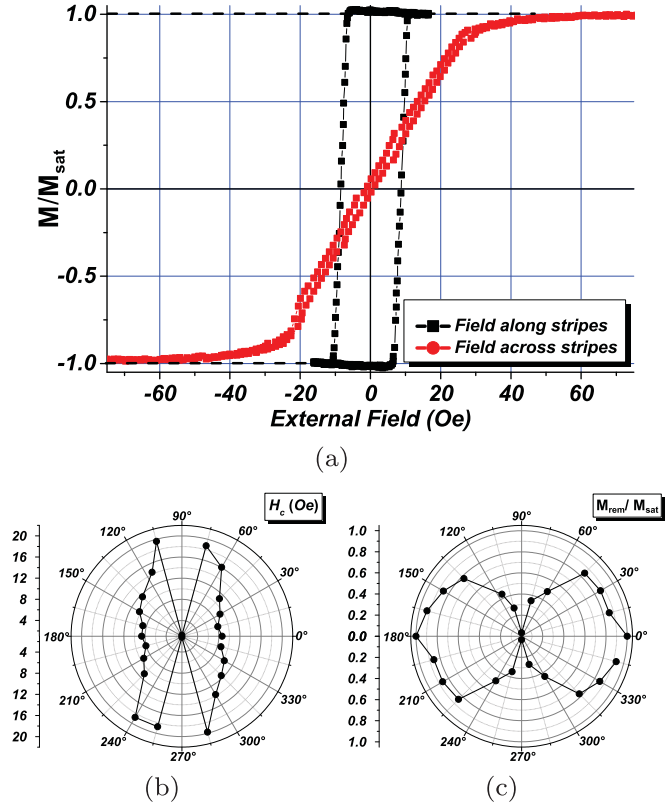

FIG. 5. Same as Fig. 4, but for the sample S2.

patterned. The patterned area covers about 85% of the total substrate area, which is confined within the red frame in Fig. 3(d). The remaining 15% at the rim consists of the bare uncovered Si substrate. Consequences of this design for PNR measurements in grazing incident geometry are discussed further below.

C. Magnetic characterization of samples

Preliminary magnetic characterization of both samples was performed by means of longitudinal magneto-optic Kerr effect (L-MOKE) hysteresis loop measurements. The sensitivity of the MOKE-installation was adjusted to the magnetization component parallel to the magnetic field applied within the sample plane at different angles to the stripes. Results of L-MOKE measurements for the S1 and S2 samples are shown in Figs. 4 and 5, respectively. Hysteresis loops recorded by applying magnetic fields along and perpendicular to the stripes are combined in Figs. 4(a) and 5(a), while panels (b) and (c) represent azimuthal dependencies of the coercivity H_c and normalized remanent magnetization $M_{\rm rem}/M_{\rm sat}$ values extracted from the hysteresis loops.

Both samples show a well pronounced shape-induced uniaxial in-plane anisotropy with easy magnetization axis (EA) oriented parallel to the stripes. Square-like open hysteresis loops measured in the EA direction show coercivity values $H_c^{\rm EA}$ equal to 57 and 9 Oe for the S1 and S2 samples, respectively. Corresponding saturation fields for the two patterns are $H_{\rm sat,S1}^{\rm EA} = 120$ Oe and $H_{\rm sat,S2}^{\rm EA} = 12$ Oe, respectively. In contrast, hysteresis loops recorded for magnetic fields applied in the direction perpendicular to the stripes are S-shaped and show negligible coerciveness of a few Oersted only for both samples. In-plane magnetic field values required for turning the magnetization vector orthogonal to the stripe array are $H_{\rm sat,S1}^{\rm HA} = 1000$ Oe and $H_{\rm sat,S2}^{\rm HA} = 60$ Oe for the samples S1 and S2, respectively.

It is well established [3,4,21] that the coercive field $H_c^{\rm EA}$ for a single isolated stripe scales with the aspect ratio t/w between stripe thickness t and widths w. Since in our case both stripe patterns have approximately the same thickness $t_1 \approx t_2$, the coercive fields should scale according to their width. The coercive field ratio $H_{c,S1}^{\rm EA}/H_{c,S2}^{\rm EA} \approx 6.3$ agrees reasonably well with the expected ratio $w_2/w_1 \approx 7.1$, considering that edge roughness and interstripe interaction is not taken into account.

The structural and magnetic parameters of both stripe arrays are listed in Table I for later reference.

IV. EXPERIMENTAL CONDITIONS FOR POLARIZED NEUTRON SCATTERING FROM MAGNETIC STRIPE ARRAYS

A. Instrumental details

For exploring edge roughness effects by off-specular scattering a set of PNR and OSS experiments were performed

TABLE I. Structural and magnetic parameters of samples S1 and S2, t is the layer thickness, w is the stripe width, d is the period of the stripe arrays, H_c is the coercive field along the stripes, $H_{\rm sat}^{\rm EA}$ is the saturation field parallel to the stripe direction, and $H_{\rm sat}^{\rm HA}$ is the saturation field perpendicular to the stripe direction.

	t (Å)	w (μm)	d (μm)	H_c (Oe)	$H_{\rm sat}^{\rm EA}$ (Oe)	$H_{\rm sat}^{\rm HA}$ (Oe)
S1	360	1.1	4	57	120	1000
S2	370	7.8	13.5	9	12	60

with the microstripe arrays S1 and S2 using the Super-ADAM polarized neutron reflectometer [45] situated at the Institut Laue-Langevin in Grenoble, France. The instrument operates at a constant wavelength $\lambda = 4.41$ Å with a wavelength spread $\Delta\lambda/\lambda = 0.7\%$ and an angular divergence of the incident beam $\Delta\alpha_i \approx 0.2$ mrad. At each glancing angle of incidence $0 < \alpha_i < 50$ mrad the scattered intensity was recorded via a 2D position sensitive detector (PSD) covering about the same range of glancing scattered angles α_f with an uncertainty $\Delta\alpha_f \approx 0.3$ mrad in the horizontal (x, z) scattering plane. In the vertical plane perpendicular to the scattering plane, the incident beam was focused at the sample position providing a divergence $\Delta\theta_y \sim 50$ mrad in angles θ_y. In addition, the measurements were performed by alternating the sign of the incident polarization with a efficiency of about 98%. Measurements of the sample S1 were performed without polarization analysis. For the sample S2, polarization analysis of scattered neutrons was accomplished with a wide-angle supermirror analyzer [46] covering all angles of acceptance by the PSD with an efficiency of about 99%. As already mentioned, the scattering plane is horizontal and polarization axis is parallel to the y direction, perpendicular to the scattering vector Q in the (x, z) plane. All measurements were performed at room temperature.

B. Remarks on the scattering conditions

The data were collected in two complementary geometries with stripes oriented perpendicular and parallel to the scattering plane as sketched in Figs. 6(a) and 6(b), respectively. The main reason for using these two geometries is the fact that at shallow angles the coherence ellipsoid mostly defined

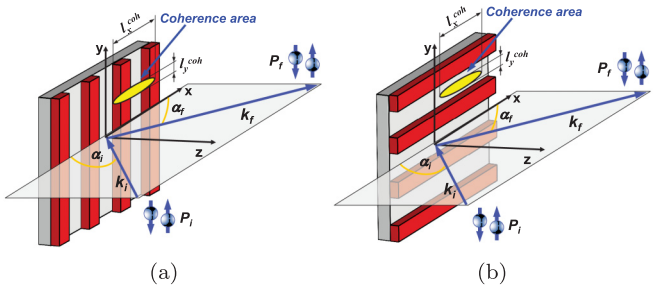

FIG. 6. Mutual orientations of the coherent ellipsoid and the array of microstripes. (a) The coherence area spans several stripes and off-specular Bragg diffraction can be observed. (b) The coherence area is collinear with the stripes, resulting in solely specular reflection for the case of *homogeneous* induction between the stripes with ideally flat edges.

by uncertainties $\Delta\alpha_i$, $\Delta\alpha_f$, $\Delta\theta_y$, and by the wavelength λ is strongly anisotropic. The coherence ellipsoid defines the volume in real space, for which constructive interference is possible. Therefore the observed scattering cross section results from different procedures of averaging over the sample surface, providing different and mutual complementary types of information on the system.

The long axis of the coherence ellipsoid $l_x^{\rm coh} \sim 2\pi/\Delta q_x$ is determined by the uncertainty Δq_x in the lateral projection q_x of the wave vector transfer $\mathbf{q}$ and can be estimated as

$$l_x^{\rm coh} \sim \frac{\lambda}{\sqrt{(\alpha_i \Delta\alpha_i)^2 + (\alpha_f \Delta\alpha_f)^2}}. \tag{1}$$

Under experimental conditions described above, the length $l_x^{\rm coh}$ ranges from a fraction of a millimeter down to a few micrometers.

The short axis of the coherence ellipsoid is determined by the uncertainty Δq_y in the wave vector transfer component q_y and this is much higher than Δq_x. Thus the short axis is estimated as $l_y^{\rm coh} \sim \lambda/\Delta\theta_y \ll l_x^{\rm coh}$ and does not exceed 10 nm.

The length $l_z^{\rm coh} \sim \lambda/\sqrt{(\Delta\alpha_i)^2 + (\Delta\alpha_f)^2}$ of the third axis is determined by the uncertainty Δq_z in the wave vector transfer q_z normal to the surface. It is estimated to be in the order of a fraction of micrometer, and hence $l_y^{\rm coh} \ll l_z^{\rm coh} \ll l_x^{\rm coh}$.

1. Perpendicular orientation

For orientation of the stipes perpendicular to the scattering plane, as depicted in Fig. 6(a), the large extension of the coherence volume $l_x^{\rm coh}$ covers a number of patterned elements. This is a prerequisite for coherent enhancement of scattering amplitudes whenever the Bragg equation $q_x = 2\pi n/d$ is satisfied, where the integer n enumerates the order of Bragg diffraction.

At a given shallow incident angle $\alpha_i > 0$ Bragg scattering is excited when the shallow scattering angle $\alpha_f = \alpha_-^B > 0$, where

$$\alpha_-^B \approx \sqrt{\alpha_i^2 - 2n\lambda/d} > \alpha_i, \tag{2}$$

with integer $n < 0$. Alternatively, Bragg conditions are satisfied when $\alpha_i = \alpha_+^B$, where

$$\alpha_+^B \approx \sqrt{\alpha_f^2 + 2n\lambda/d} > \alpha_f, \tag{3}$$

with $n > 0$.

Note that at $n = 0$ these equations merge with the Snell's law $\alpha_f = \alpha_i$ for specular reflection. Its amplitude is determined by the mean scattering length density (SLD) averaged over the coherence ellipsoid. Such averaging is quite straightforward if a saturating magnetic field is applied along the stripes. Then, due to the Zeeman splitting of the neutron spin state by the magnetic induction in the stripes, the SLD $Nb^{\pm} = Nb_n \pm Nb_m$ is split in accordance with the positive or negative spin projection onto the field direction. Here, N is the nuclear number density, b_n is the coherent nuclear scattering length, and b_m is an effective magnetic scattering length.

As the external field within the stripes and in the ISS does not cause scattering contrast, we conclude that in the case of perpendicular orientation of stripes with ideal edges the mean SLD value is given by $\overline{Nb}^{\pm} = \eta Nb^{\pm}$, where $\eta = w/d$

is the surface fraction covered by the stripes. These reduced mean SLDs are used to calculate the reflection amplitudes $r = r^{\pm}$ for each of the spin states. Then non-spin-flip (NSF) and spin-flip (SF) scattering cross sections and corresponding reflection coefficients, $R^{\pm\pm}$ and $R^{\pm\mp}$, expressed [42–44] via bi-linear combinations of reflection amplitude $r^{\pm}$ and its complex conjugated value $r^{\pm *}$ are averaged over incident and outgoing spin states filtered by the polarizer and analyzer. The result is finally convoluted with the 3D resolution function and incoherently averaged over all coherence ellipsoids covering the whole sample surface. As soon as each of the coherence ellipsoids crosses many stripes, then the mean values of SLDs in saturation are almost independent of the lateral coordinate and incoherent averaging of reflectivities over different ellipsoids is trivial.

In short, in perpendicular orientation OSS at shallow angles provides information on width and periodicity of stripe arrays and on magnetic induction within the stripes. In this orientation OSS is, however, less sensitive to edge roughness and the resulting magnetic flux in the interspace between the stripes. Therefore a complimentary orientation has to be chosen to supplement with the remaining information. This is done by the parallel orientation, discussed next.

2. Parallel orientation

In order to match the edge roughness correlation length with the long axis of the coherence ellipsoid, the samples have to be rotated by 90° about the surface normal. In this parallel orientation sketched in Fig. 6(b), no Bragg diffraction can be seen as neither of coherence ellipsoids crosses more than a single stripe. Then neutron waves scattered from different stripes do not interfere. Also there is almost no interference between waves reflected from the stripes and ISS's filled with magnetic field: only very few coherence ellipsoids cover the stripe edge area and hence the fraction of neutron beam hitting stripe edges is negligible. Even in the case of rough edges it remains small if $\sigma_e \ll d$, where σ_e is the rms edge roughness. Therefore, the specular reflection coefficients $R^{\pm}$ can be represented as an incoherent sum of reflectivities from individual stripes $R_s^{\pm}$ and reflectivities $R_i^{\pm}$ from the ISS weighted with the corresponding surface factors η and $(1-\eta)$, respectively,

$$R^{\pm} = \eta R_s^{\pm} + (1-\eta) R_i^{\pm}. \tag{4}$$

As already mentioned, the small volume occupied by edge roughness does not allow to directly detect off-specular scattering from fluctuations of the nuclear scattering potential associated with this roughness. However, due to the continuity of magnetic flux lines in the ISS even relatively small edge roughness may substantially perturb the magnetic field homogeneity over a large distance between neighboring stripes, as sketched in Fig. 1(b). This is particularly true if a saturating external field is applied perpendicular to stripe edges. In the following, we assume that the magnetization within stripes is homogeneous up to their boundaries with vacuum. In case of statistical edge roughness these boundaries may be approximated by a sequence of small flat segments randomly tilted with respect to the mean edge surface averaged over roughness. Consequently, each of those segments may be characterized by the unit vector $\boldsymbol{n}_i$ normal to its surface and making a certain angle β_i with the mean field direction averaged over all angles β. Magnetic induction $\boldsymbol{B}_i$ induced in the interstripe space by magnetization $\boldsymbol{M}$ and crossing the segment surface is directed along the vector $\boldsymbol{n}_i$. In particular, for the case presented in Fig. 1(b) the unit vector $\boldsymbol{n}_i$ is collinear with the corresponding vector component $\boldsymbol{B}_{\perp,i}$ of the magnetic induction in the interstripe space, while the direction of the mean induction coincides with the external field direction $\boldsymbol{H}_{\text{ext}}$.

Summing up, both orientations are needed for a complete analysis of the stripe patterns. The perpendicular orientation holds for an overall assessment of the geometry of the stripe array, including stripe width and periodicity, whereas the parallel orientation adds information on the magnetic flux distribution in the interspace region affected by edge roughness.

V. EXPERIMENTAL PNR AND OSS RESULTS

A. Sample S1

1. Perpendicular orientation of sample S1

The PNR results on the sample S1 with stripes oriented perpendicular to the scattering plane and collinear with the incident polarization are combined in Fig. 7. An external field of 5.2 kOe was applied along the y axis, collinear to the stripes and to the neutron polarization vector, and then reduced to the field of $H_{ext} = 100$ Oe. In this orientation, the coherence ellipsoid with the long axis l_x^{coh} intersects many stripes as indicated in Fig. 6(a) providing conditions for observing Bragg diffraction.

In Fig. 7(a), the specular reflectivities R^+ and R^- with polarization directed along with, or opposite to the applied field are plotted together with the least-square fit of the data to the model. Input model parameters are chosen in accordance with the sample preparation procedure and structure characterization described in the previous section. Refined values are determined by applying least square routine to fit simultaneously both reflectivity curves R^+ and R^- in one go. Among the salient features of these reflectivities one may note an appreciable splitting of the curves for different spin states and for angles above the critical angle $\alpha_c^{\text{Si}} \approx 3.5$ mrad of total reflection from the silicon substrate. This feature confirms that the sample contains a magnetic layer magnetized in the field of 100 Oe. However, the magnetization is not strong enough to be expressed in a splitting of the critical edges due to the Py stripe array. This may also be due to the fact that the layer is not sufficiently thick so that neutron waves tunnel through the layer and then totally reflect from the substrate. We come back to this point in the next subsection, where we compare the critical edges for parallel and perpendicular alignment. The magnetic layer thickness can be roughly estimated from the period of interference fringes observed in both curves R^+ and R^-.

Taking into account the nominal sample structure and the arguments mentioned above, the final refinement is accomplished for the model consisting of three effective layers on the substrate, as illustrated with the SLD depth profile in Fig. 7(b). Each layer is characterized by four parameters: layer thickness t, interface rms roughness σ, the mean value of nuclear SLD $\overline{Nb_n}$ and mean induction $\overline{B}$. The resulting fit parameters are listed in the first three and in the fifth column of the Table II.

TABLE II. Fit parameters extracted from the fit of specular reflectivity curves shown in Fig. 7 for the sample S1 with stripes oriented perpendicular to the scattering plane and field of $H_{\rm ext} = 100$ Oe applied parallel to the stripes. t is the layer thickness and σ is interface rms roughness. The other parameters are explained in the text.

	t (Å)	σ (Å)	$\overline{Nb_n}\ 10^{-6}$ (Å^{-2})	$Nb_n\ 10^{-6}$ (Å^{-2})	$\overline{B}$ (kG)
Cr cap layer	24.5	6.1	0.82	2.98	0
Py layer	359.8(5)	10.4(7)	2.50(1)	9.09	2.98(1)
Ti seed layer	9.5(2)	4(2)	−0.53	−1.93	0
Si substrate	–	2.2	2.14(1)	–	0

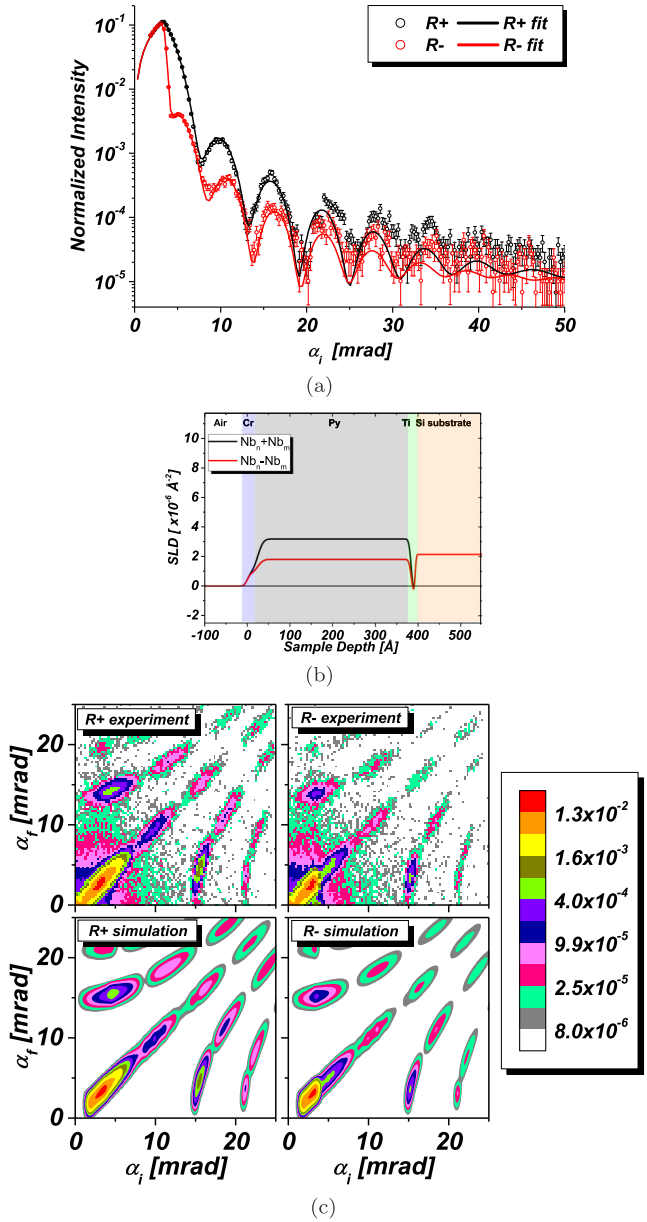

FIG. 7. (a) Specular reflectivities R^+ and R^- (open circles) together with best fit of the experimental data (solid lines) for stripes S1 oriented perpendicular to the scattering plane in the field of $H_{\rm ext} = 100$ Oe applied parallel the stripes. (b) Nuclear and magnetic SLD profiles extracted from the fit. (c) Experimentally recorded off-specular scattering maps for up and down polarized neutrons (top) and corresponding model calculation (bottom).

From Table II follows that the permalloy layer thickness is close to the nominal value in Table I, while rms interface roughness is small. One can also compare the nuclear SLD fit parameters with the expected values. This can be done by taking into account the filling factor determined from SEM images (shown in Fig. 2) as $\eta = 0.275$. Then, using the experimentally determined mean value of nuclear SLD $\overline{Nb_n}$ from the fit, the nuclear SLD of the stripe material can be evaluated according to $Nb_n = \overline{Nb_n}/\eta$. Both values, $\overline{Nb_n}$ and Nb_n, are listed in Table II in the third and forth column, respectively. For example, the recalculated SLD of permalloy is found to be equal to $Nb_n = 9.09 \times 10^{-6}$ Å^{-2}, which is very close to its nominal value 9.12×10^{-6} Å^{-2} for permalloy $Fe_{22}Ni_{78}$. The SLD of chromium determined from the fit is slightly lower than the nominal value 2.99×10^{-6} Å^{-2}. Similarly, the negative SLD value of titanium is close to its nominal value -1.95×10^{-6} Å^{-2}.

The mean magnetic induction in the fifth column is recalculated from the experimentally determined magnetic SLD $\overline{Nb_m}$ of the effective permalloy layer according to the equation

$$B\ [\mathrm{G}] = \frac{2\pi\hbar^2}{m_n^*\mu_n} Nb_m = \frac{Nb_m[10^{-6}\ \text{Å}^{-2}]}{2.312} \times 10^4, \qquad (5)$$

where m_n^* is the neutron mass and μ_n is its magnetic moment.

From the fit it follows that in an external field of 100 Oe the mean magnetic induction of the permalloy effective layer is close to 3 kGauss. This value represents the mean induction averaged over the coherence ellipsoid crossing a number of stripes with its long axis. Correspondingly, the mean induction is reduced from that of a Py continuous layer due to the same filling factor $\eta = 0.275$ as applied for the nuclear SLD of all layers. Then the magnetic induction of the continuous film at this field is expected to be 10.85 kG. This is also very close to what is expected for bulk $Fe_{22}Ni_{78}$ permalloy (9.95 kG) with a slight excess of Fe.

It should be noted that pronounced Kiessig fringes can be observed in the specular reflectivity scans although the stripe array constitutes an effective roughness equivalent to the thickness of the stripes. This becomes possible due to the grazing incidence geometry of the experiment, whenever the coherence ellipsoid in the z direction is larger than the thickness of the film. Then neutron waves, scattered from stripes and from free space between the stripes, are added coherently, resulting in a decrease of the mean scattering potential, while maintaining the potential steps at the surface and at the interface responsible for the interference effects. At the same time, the true interface roughness of individual stripes remains constant and small, on the order of several

angstroms, and thus interference from well defined sharp interfaces results in deep and distinct Kiessig oscillations.

One may notice that the quantitative analysis of specular PNR already delivers almost the whole set of parameters characterizing the structural and magnetic properties of the stripe pattern. However, the analysis so far does not prove the general concept of the surface averaging procedure applied to treat PNR data and does not determine the lateral period and the surface factor of stripes. This can be achieved via the analysis of the OSS, including off-specular Bragg diffraction measured simultaneously with specular PNR.

The upper row of the Fig. 7(c) shows two experimental OSS maps for the polarization parallel and antiparallel to the external field guiding neutron polarization to the sample. The bottom row shows corresponding maps simulated in the distorted wave born approximation (DWBA) [42–44], where neutron wave functions are calculated for mean layer SLDs averaged over coherence ellipsoids, while the periodic structure is considered as a perturbation. Hence the simulations are based on parameters deduced from fits of corresponding specular reflectivity curves shown in the Fig. 7(a) and were performed adjusting only two additional parameters: the stripe width w and the period d of the stripe array. Diagonal ridges seen in the intensity maps for angles $\alpha_i = \alpha_f$ represent the specular reflectivity from the mean scattering length density $\overline{Nb}$ averaged over the lateral structure. Curved bands displayed on both sides of the specular reflection ridge correspond to off-specular Bragg diffraction from the stripe pattern with a lateral period of $d = 4$ μm. These bands are well visible up to the second order. Thus the assumption of stripes with rectangular shape and width $w = 1.1$ μm together with the set of parameters listed in Table II reproduces very well the intensity distribution over different orders of lateral Bragg reflections without any additional scaling to specular ridges. This provides strong evidence in favor of the general approach to data treatment and confidence to its results.

2. *Parallel orientation of sample S1*

Now we consider PNR results from the sample S1 with stripes oriented parallel to the scattering plane as sketched in Fig. 6(b). An external saturating field of 1 kOe was applied parallel to the y axis and perpendicular to stripe array. According to the hysteresis loop plotted in Fig. 4(a) the field of 1 kOe is sufficient to almost fully saturate the magnetization of the sample. Specular reflectivity scans and intensity maps are combined in Fig. 8 together with fits, corresponding SLD profiles and simulations.

The specular reflectivity curves presented in the Fig. 8(a) show thickness oscillations with about the same period as in Fig. 7(a), but in contrast to the latter, the oscillations in R^+ are now appreciably phase shifted with respect to those in R^-. Moreover, at low angles PNR curves in Figs. 7(a) and 8(a) exhibit different behavior although reflectivities R^+ and R^- in both figures reveal sharp peaks at the positions close to the critical angle of the silicon substrate $\alpha_c^{\mathrm{Si}} \approx 3.5$ mrad. Curves R^+ and R^- shown in Fig. 7(a) steeply decay with different rates at $\alpha_i \geqslant \alpha_c^{\mathrm{Si}}$. This difference in slope is due to the fact that, in accordance with the SLD profile in the Fig. 7(b), the SLD for negative spin component is smaller than that of Si,

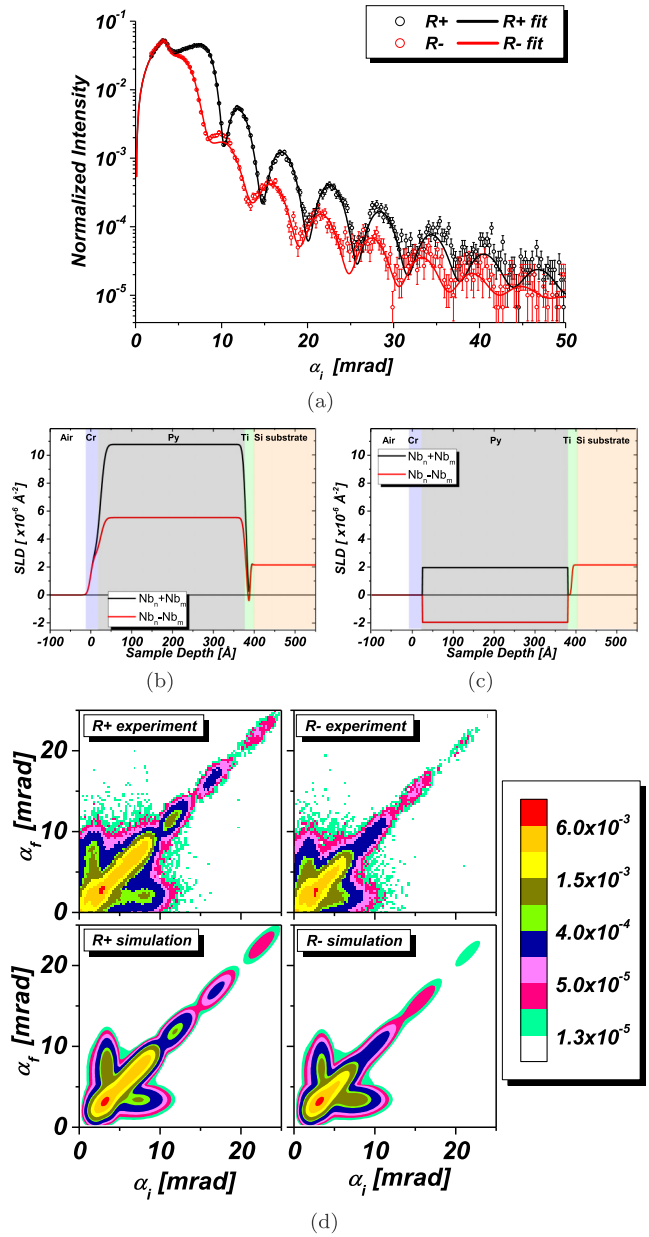

FIG. 8. (a) Specular reflectivities R^+ and R^- (open circles) together with best fit of the experimental data (solid lines) for stripes S1 oriented parallel to the scattering plane in the field of $H_{\mathrm{ext}} = 1$ kOe applied perpendicular to the stripes. (b) SLD profile describing the reflectivity from the stripe stack weighted in the fit with the surface factor $\eta = 0.39$. (c) SLD profile describing the reflectivity from the interstripe space, weighted in the fit with the surface factor $1 - \eta = 0.61$. (d) Corresponding off-specular scattering maps with simulations.

and hence the critical angle α_c^- for spin-down neutrons is slightly lower than the angle α_c^{Si}. As a result, the corresponding critical edge for this spin component is hidden. For the positive spin component the SLD is higher than the SLD of the substrate and the angle α_c^+ is a bit higher than α_c^{Si}. However, the extinction length is larger than the layer thickness and reflection within the range $\alpha_c^{\mathrm{Si}} < \alpha_i < \alpha_c^+$ is not total.

TABLE III. Parameters extracted from the fit of specular reflectivity curves plotted in Fig. 8(a) for stripes parallel to the scattering plane in a field of $H_{\rm ext} = 1$ kOe applied perpendicular to the stripes. Some cells show two values. The upper values correspond to the stripe materials, while the bottom ones refer to the interstripe space. t and σ are film thickness and interface roughness, respectively. The remaining parameters are explained in the text.

	t (Å)	σ (Å)	Nb_n 10^{-6} (Å^{-2})	B (kG)
Cr cap layer	24.5(7)	6.1	2.7	0
		0	0	
Py layer	356.2(3)	9.1(5)	8.13(1)	11.25(3)
		0	0	8.44(3)
Ti seed layer	9.7	6.1(3)	−1.74	0
		0	0	
Si substrate	–	2.2	2.14(1)	0
$\langle\cos\Delta\gamma\rangle_{\rm coh}$			1	
			0.75	
$\langle\cos\overline{\gamma}\rangle_{\rm inc}$			0.98(1)	
			0.3	
stripe surface factor η			0.39(1)	

In contrast to Fig. 7(a), the reflectivity R^+ in Fig. 8(a) reveals an additional maximum $\alpha_i \approx \alpha_c^+$ corresponding to the critical angle $\alpha_c^+ \approx 7.8$ mrad for the positive spin component from the permalloy film. The angle of total reflection $\alpha_c^- \approx 6$ mrad for the negative spin component is manifested by a step, or "shoulder," on the reflection curve R^- and a subsequent steep descend. In both cases, the critical edges are smeared out due to the finite thickness of the permalloy layer.

The visibility of two critical angles $\alpha_c^\pm$ of permalloy simultaneously with the critical angle of silicon $\alpha_c^{\rm Si}$ suggests that the reflectivity curves displayed in Fig. 8(a) are described by Eq. 4 in which one pair of reflectivities, $R_s^\pm$, is due to reflection from the trilayer consisting of the cap layer, permalloy stripes and seed layers on the substrate, while the other, $R_i^\pm$, originates from the bare substrate in between of the stripes. Such model, however, does not describe correctly the amplitudes of the R^+ and R^- reflectivity oscillations and the phase shift between these oscillations as seen in Fig. 8. This discrepancy is immediately removed by calculating reflectivities $R_i^\pm$ for the same model as used for $R_s^\pm$ in which the Ti/Py/Cr trilayer is substituted by an "effective layer" of magnetic induction on top of the substrate with no material ($Nb_n = 0$).

Results of the fit are shown by the solid lines in the Fig. 8(a), while the SLD profiles for stripes, $Nb = Nb_s$, and for ISS, Nb_i, are illustrated in the Figs. 8(b) and 8(c). Note that the SLD of the stripe stack in Fig. 8(b) is positive everywhere except of a narrow range of titanium layer next to the substrate.

In contrast, the SLD value of the ISS is negative for negative spin projection onto the interstripe field direction providing a phase shift between oscillations in R_i^- and R_i^+. For comparison, the calculated partial reflectivities $R_{s,i}^\pm$ are shown in Ref. [47].

The extracted fit parameters are listed in the Table III. Layer thicknesses and interface roughnesses collected in the first and second columns of this table agree well with the values determined above for the perpendicular stripe orientation. Upper and lower lines in the table cells refer to the stripe material and the empty interstripe space, respectively. The nuclear SLDs of the stripes $Nb_n = Nb_n^s$ are quoted in the third column, upper lines of cells, while the interstripe SLDs $Nb_n = Nb_n^i$ are fixed to zero, as no material is expected between stripes. The magnetic induction in the stripes and in the interstripe space is listed in the 4-th column. Further parameters discussed below are listed in an additional panel at the bottom.

Inspecting the set of parameters in Table III, one may notice that the absolute values of nuclear SLDs are systematically lower than their nominal values by about 10%. At the same time, the surface fraction $\eta = 0.39$ determined from the fit is appreciably higher than the value $\eta = 0.275$ extracted from SEM images and confirmed by PNR results in the previous subsection. Both effects can be explained by the edge roughness. In case of no roughness, the major part of the coherence ellipsoids with their longest axis parallel to stripes lie either completely within the stripes or fall into the ISS, as depicted in Fig. 6(b). At the same time, only a small percentage of ellipsoids determined by the ratio $l_y^{\rm coh}/d \sim 0.25\%$ covers the stripe boundaries. The mean value of nuclear SLD averaged over such ellipsoids is reduced and the stripe width is effectively increased. However, the overall effect is too small to be detected in the present experiment.

The effect of the edge smearing substantially increases if stripe edge roughness is as high as 0.1 μm, as estimated from SEM images in Fig. 2. Then the effective stripe width increases by about 10%–20% along with simultaneous decrease of the mean SLD. Unfortunately, it is not possible to estimate these effects more accurately within the simple model used in the PNR fit, because introducing extra parameters characterizing edge roughness does not improve the fit quality. Moreover, such parameters are highly sensitive to misalignments such as an in-plane tilt angle χ between stripes and longest axes of coherence ellipsoids, also resulting in a SLD reduction.

The precision of the χ angle required for probing the edge roughness and the effect of the SLD reduction, connected with a misalignment of the χ angle, are briefly discussed in Appendix A. However, it should be reminded that the primary goal of this work is not to study the edge roughness with PNR, but instead, our attention is mostly concentrated on the magnetic effects caused by edge roughness.

One of the main effects of edge roughness consists in an appreciable reduction of the mean interstripe magnetic induction $B = B_i$ (fourth column in Table III, bottom line) relative to the stripe induction $B = B_s$ (upper line) found close to its saturation value $B^{\rm sat}$. The reduction of the mean induction $B_{s,i}$ is due to the tilt angles $\Delta\gamma = \Delta\gamma_{s,i}$ between flux lines within coherence ellipsoids and the field direction averaged over coherence volume. Corresponding reduction factors denoted as $\langle\cos\Delta\gamma\rangle_{\rm coh} = B_{s,i}/B^{\rm sat} \leqslant 1$ are given in two first rows of the subtable in Table III. The directions of mean induction averaged over different coherence ellipsoids are, however, not necessary parallel to the external field, but may be tilted for angles $\overline{\gamma} = \overline{\gamma}_{s,i}$ varying over large distances, see, i.e., Fig. 11. The result of additional incoherent averaging over all ellipsoids is characterized by another two parameters $\langle\cos\overline{\gamma}\rangle_{\rm inc} = \langle\cos\overline{\gamma}_{s,i}\rangle_{\rm inc} \leqslant 1$ indicated in last rows of the subtable. The physical significance of these parameters, as well as

the need for two types of fit parameters [42–44] describing the specular reflectivity data is dictated by the specifics of the two-step surface averaging, discussed in more detail in Appendix B.

Both types of parameters were freely varied during the fitting procedure, while the saturation induction $B^{\rm sat}$ was fixed to the value indicated in the upper row of the fourth column of the main Table III. The stripes are close to the saturation state so that $\langle\cos\Delta\gamma_s\rangle_{\rm coh} = 1$ and $\langle\cos\overline{\gamma}_s\rangle_{\rm inc} = 0.98$, whereas the induction in between the stripes is reduced by both factors: $\langle\cos\Delta\gamma_i\rangle_{\rm coh} = 0.75$ and $\langle\cos\overline{\gamma}_i\rangle_{\rm inc} = 0.3$. As a result, the net value of interstripe induction, reduced by the product of the two latter factors, amounts to only 22.5% of the stripe induction.

One possible explanation for the observed reduction of the interstripe induction and hence of the magnetic SLD may be due to magnetic flux straying from stripe edges into the outer space in the z direction. However, our best fit does not detect any magnetic induction above and below the layer containing permalloy. This confirms the assumption that the vector $\boldsymbol{B}$ is mostly confined between the top and bottom boundaries of the permalloy stripes having only two components $B_x = B\sin\gamma$ and $B_y = B\cos\gamma$, where γ is the in-plane homogeneous tilt angle of the vector $\boldsymbol{B}$ with respect to applied field. These tilts may occur, for instance, if the external field is applied not precisely normal to stripes. Then in the case of a moderate applied field amplitude even a small misalignment between the field direction and the stripe edges may cause appreciable tilt angles $\gamma_{s,i}$ due to the stripe demagnetization factor. As a result, the magnetization vector may flip almost along the stripes. However in our case such a scenario was not observed and the magnetic induction in stripes was well parallel to the externally applied field which is sufficiently strong to overcome a global demagnetizing field of the stripes.

An alternative and more plausible explanation of the appreciable reduction of the projections $B_y^{s,i}$ suggests that the angle $\gamma_{s,i}$ is *randomly* distributed over the magnetic layer cross sections. Such reduction is described in our model by two types of parameters introduced above: $\langle\cos\Delta\gamma_{s,i}\rangle_{\rm coh}$ and $\langle\cos\overline{\gamma}_{s,i}\rangle_{\rm inc}$. From the Table III, it follows that the parameter $\langle\cos\overline{\gamma}_s\rangle_{\rm inc} \approx 0.98$ indicating that the tilt angle $\overline{\gamma}_s$ between the stripe magnetization and the external field direction is less than 11.5°. At the same time, the value $\langle\cos\overline{\gamma}_i\rangle_{\rm inc} \approx 0.3$ means that the interstripe magnetic induction is either tilted against the applied field direction by the angle of 72.5°, or experiences random tilt to the left and to the right with respect to this direction. In fact, from PNR data, one cannot determine the sign of the tilt angles $\overline{\gamma}_i$ and $\overline{\gamma}_s$. Moreover, using PNR with no polarization analysis of the reflected beam it is not possible to distinguish between an inhomogeneous field between stripes and a homogeneous tilt of induction with respect to the external field.[1] However, since the angle $\overline{\gamma}_s$ is small, there is no reason to expect that the direction of interstripe induction is homogeneously tilted. It is more likely that it experiences random inhomogeneous tilts due to edge roughness as sketched in Fig. 1(b).

[1]This question can be clarified using the polarization analysis which provides access to the mean square $\langle\sin^2\overline{\gamma}_{s,i}\rangle$.

Assuming a self-affine edge roughness, one may suppose that notches possess an internal fractal-type self-similar structure, a fragment of which depicted in Fig. 1(b) mimics the result of averaging over the coherence volume. The same refers to the flux lines along which the tilt angle $\overline{\gamma}_i = \overline{\gamma}_i(x, y)$ smoothly varies between zero in the middle of the ISS and the maximum value $\gamma_{\max}(x, y)$ determined by the magnetic flux continuity boundary conditions. So in Fig. 1(b) $\gamma_{\max}(x, y) \approx \pm 90°$ directly at notches, while $\gamma_{\max}(x, y) \approx 0°$ between them. The low experimental value $\langle\cos\overline{\gamma}_i\rangle_{\rm inc} \approx 0.3$ means that there are no flat segments between notches and the interface x profile is rather sawtooth like shaped.

Recall that the PNR measurements in our case are not sensitive enough to the structural part of edge roughness observed by electron microscopy because of lack of scattering volume and resolution in the y direction. However, edge roughness can be made noticeable to neutron scattering indirectly. In high external magnetic fields, edge roughness invokes extensive inhomogeneous stray fields in the interspace region between the stripes, as discussed in Sec. IV B 2. Such inhomogeneous fields generate spin-dependent OSS as can be clearly seen in the maps displayed in the Fig. 8(d) for stripes oriented parallel to the scattering plane. The latter statement is supported by simulations of OSS maps carried out within the framework of DWBA [42–44] and displayed below the experimental maps in Fig. 8(d). The simulations reasonably well reproduce the basic features of OSS without any special scaling to the specular reflected intensity. In both sets of maps, one can see the specular ridges running along the diagonal $\alpha_i = \alpha_f$ similar to those in Fig. 7(c), but without curved Bragg bands approaching this ridge at higher incident and scattered angles. Instead, a pair of petal shaped diffuse intensity lobes are visible on both sides of the ridge. The diffuse intensity is enhanced in the vicinity of the critical edges of specular reflection from the "effective layer" of mean interstripe induction. This intensity enhancement is due to the Yoneda effect [48].

Alternative maps are shown in Ref. [47]. These maps were simulated by the same theoretical model as stated above, but assuming zero induction $B_i = 0$ between the stripes. Obviously, in this case no off-specular diffuse scattering exists.

The theoretical model used for simulating the OSS maps in the frame of DWBA is discussed in detail in Appendix C. In brief, the general idea of DWBA is based on the separation of the interaction potential, U into two parts [49]: $U = U_0 + \Delta U$. The main part U_0 is chosen to provide an exact solution of the wave equation, while the remaining part, $\Delta U = U - U_0$, is accounted for as a perturbation providing corrections to the reference exact solution. In case of shallow incidence of neutron wave onto a laterally modulated film, the choice of reference potential is quite obvious. This is the mean value $U_0 = \langle U\rangle$, laterally averaged over the coherence volume if the latter contains a number of lateral heterogeneities. Such a reference $1D$ potential is independent of the in-plane coordinates providing specular reflection from and refraction into the effective film. It is also responsible for optical distortions of neutron waves propagating inside the mean potential. In the second stage of DWBA, the scattering amplitude of distorted waves from deviations, $\Delta U = U - \langle U\rangle$, is calculated in the first (Born) order of the perturbation theory. It is very

important that in this version of DWBA the approximate perturbation potential ΔU contributes solely to OSS, but not to specular reflection and/or refraction, as the mean value $\langle U \rangle = 0$.

Close similarity between measured diffuse maps and simulations shown in Fig. 8(d) lends credibility to the assumptions made, while the general concept of edge roughness generating OSS is further confirmed by the counter-example of measurements on the second sample S2 featuring stripes with smooth edges, to be discussed in the next section.

B. Sample S2

We will now focus our discussion on PNR measurements performed on the 370-Å-thick permalloy sample S2. In this sample the roughness of the stripe edges is much less jagged although its amplitude, and hence the rms roughness, is higher than in sample S1. As seen from SEM images in Figs. 3(b) and 3(c), the stripe edges, in contrast to those in Figs. 2(b) and 2(c), do not reveal any pronounced sharp notches or kinks on about the same submicrometer length scale. Instead, a smoothly varying waviness prevails along stripe edges. Therefore one may expect that the direction of magnetic induction vector in the interstripe space ISS) may only slightly deviate from that in the stripe body. This expectation is indeed confirmed experimentally by PNR measurements carried out on the sample S2.

In analogy to the previous measurements, two complementary orientations of coherence ellipsoids with respect to stripes were probed. An external field of 5.2 kOe was applied perpendicular to the scattering plane either along or across the stripes during data acquisition. In this set of experiments, polarization analysis was applied for specular reflectivity and off-specular scattering via recording of two NSF (R^{++} and R^{--}) and two SF (R^{+-} and R^{-+}) reflectivities. They were extracted from four maps of OSS cross-sections measured by the use of a PSD detector equipped with a wide-angle multichannel spin analyzer [46].

Specular reflectivities collected from the sample S2 with stripes oriented perpendicular and parallel to the scattering plane are plotted together with the results of best least-square fits in the Figs. 9(a) and 10(a), respectively. Each set of four reflectivity curves were fit by the theoretical model assuming two layers on a bare Si substrate. The reasons for the obvious mismatch between experimental data and fit for incident angles above 12 mrad are discussed in Sec. V B 1.

All fit parameters are combined in Tables IV and V. The NSF reflectivity curves R^{++} and R^{--} are appreciably split, signifying a well saturated state of the sample in both configurations characterized by $\langle \cos \Delta\gamma \rangle_{\rm coh} = \langle \cos \overline{\gamma} \rangle_{\rm inc} = 1$ as follows from the fit. This is also confirmed by measurements of SF reflectivities R^{+-} and R^{-+}, as well as of OSS. Observed SF effects are seen to be rather small and totally described by imperfect polarization analysis, the efficiency of which does not exceed 97%–98%.

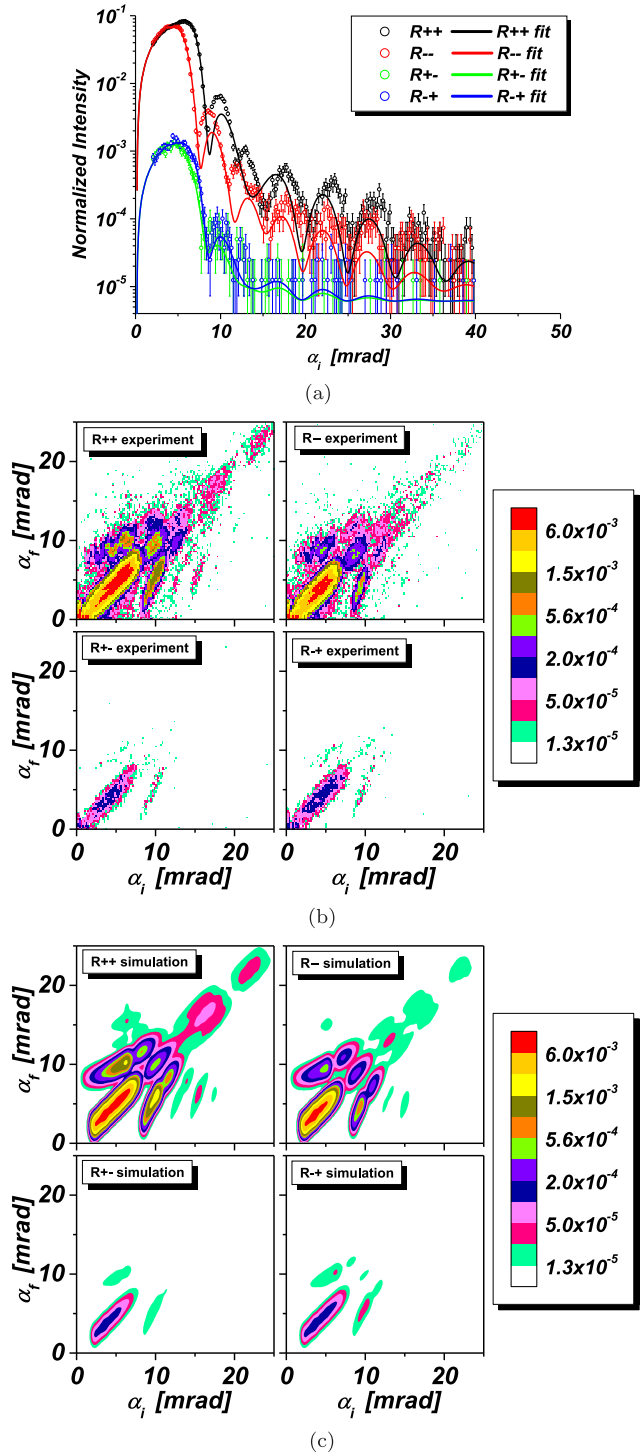

FIG. 9. (a) NSF and SF reflectivities for sample S2 with stripes oriented perpendicular to the scattering plane and in a field of $H_{\rm ext} = 5.2$ kOe applied along the stripes. Open circles are experimental data points, solid lines are best fit results. (b) Simultaneously acquired off-specular scattering maps. (c) Model calculations.

1. Perpendicular orientation of sample S2

In addition to the parameters already used for fitting the PNR data of sample S1, one more parameter $\langle \sin^2 \overline{\gamma} \rangle_{\rm inc}$ is required here to describe the specular SF reflectivity. Its value is equal to zero, as expected for the saturation state. The stripe filling factor for the perpendicular geometry is only $\eta = 0.86$ because of the sample design, which includes a narrow frame of a bare Si substrate surrounding the stripe

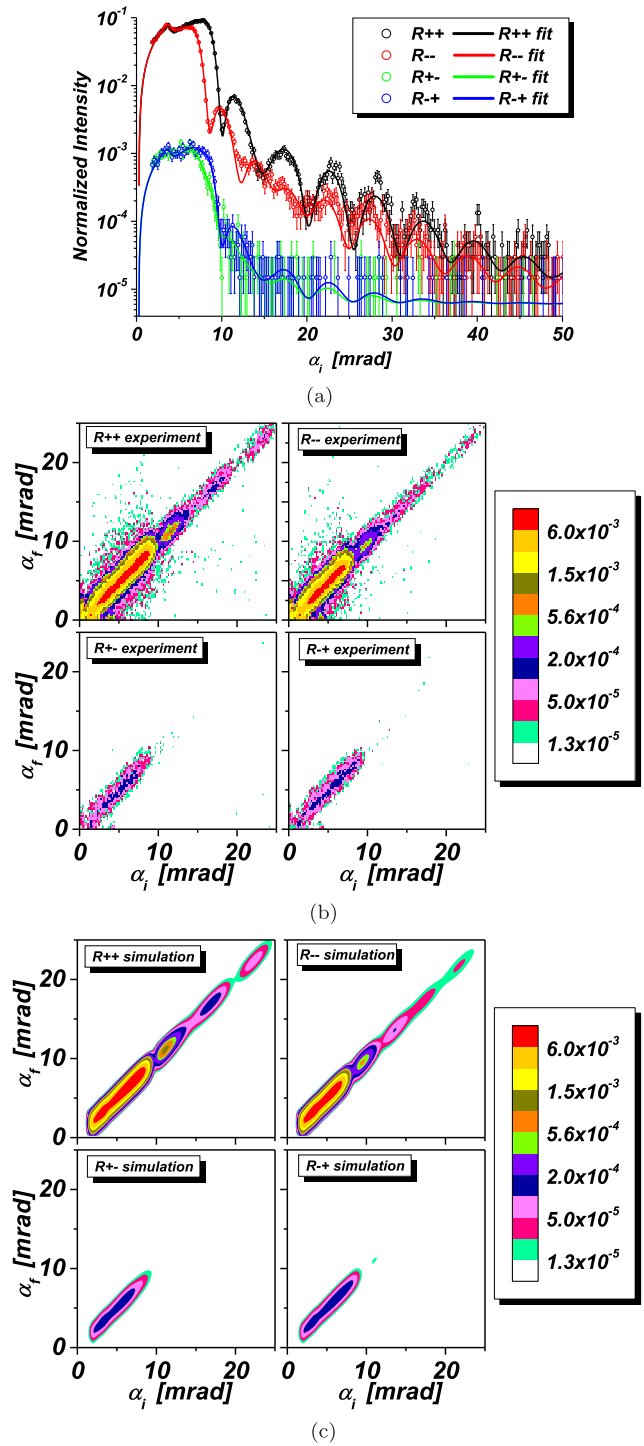

FIG. 10. Same as Fig. 9, but for the stripes oriented parallel to the scattering plane in a field of $H_{\text{ext}} = 5.2$ kOe applied across the stripes.

array pattern seen in Fig. 3(d). Because of the frame, only 14% of neutrons hitting the sample surface are reflected from the bare Si substrate. The critical edge of total reflection from silicon can be observed in both orientations of the sample S2. All other fit parameters listed in Tables IV and V have the same meaning as before for sample S1. Comparing these tables with tables II and III, one may notice that the mean

TABLE IV. Parameters extracted from the fit of the specular reflectivities shown in Fig. 9(a) for the sample S2 with stripes oriented perpendicular to the scattering plane in the field of $H_{\text{ext}} = 5.2$ kOe applied along the stripes. Data were fit with the theoretical model in which the reflectivity curves are described as an incoherent weighted sum of two reflectivity curves. Upper values in cells correspond to the first reflectivity with relative weight given by the stripe surface factor $\eta = 0.86$. Bottom values refer to the second reflectivity with relative weight of 0.14 supplementing the total surface.

	t (Å)	σ (Å)	$\overline{Nb}$ 10^{-6} (Å^{-2})	$\overline{B}$ (kG)
Pt cap layer	83.2	25.3	3.02	0
		0	0	
Py layer	370	12.7	5.45(1)	4.45(2)
		0	0	0
Si substrate	–	5.2	2.14(1)	0
$\langle\cos\Delta\gamma\rangle_{\text{coh}}$			1	
			0	
$\langle\cos\overline{\gamma}\rangle_{\text{inc}}$			1	
			1	
$\langle\sin^2\overline{\gamma}\rangle_{\text{inc}}$			0	
			0	

values of nuclear and magnetic SLDs for stripes in the S2 sample are appreciably higher than in the case of the sample S1. This is just due to the fact that the ratio of the stripe width w to the period is about 50%, while in sample S1 this ratio is only about 25%.

Panels (b) and (c) of Fig. 9 show the off-specular scattering maps for the sample S2 together with results of respective theoretical simulations. In these maps, one can clearly distinguish the off-specular Bragg bands up to third order embracing the specular ridge from both sides. However, due to larger lateral period of the S2 stripe array compared to S1 (13.5 μm versus 4 μm), the Bragg bands run closer to each other and, because of finite resolution of the instrument, merge with the specular reflectivity ridge already at the incident angle of

TABLE V. Same as Table IV, but for the sample S2 with stripes oriented parallel to the scattering plane in a field of $H_{\text{ext}} = 5.2$ kOe applied across the stripes. Upper and bottom values in the cells correspond to first and second reflectivity curves weighted by an incoherent sum with surface factors 0.58 and 0.42, respectively, for describing the experimental data.

	t (Å)	σ (Å)	Nb 10^{-6} (Å^{-2})	B (kG)
Pt cap layer	83.2(8)	25(2)	4.72(11)	0
		0	0	
Py layer	370.3(6)	13(1)	8.50(1)	7.57(3)
		0	0	7.57(3)
Si substrate	–	5.2(6)	2.14(1)	0
$\langle\cos\Delta\gamma\rangle_{\text{coh}}$			1	
			1	
$\langle\cos\overline{\gamma}\rangle_{\text{inc}}$			1	
			1	
$\langle\sin^2\overline{\gamma}\rangle_{\text{inc}}$			0	
			0	
stripe surface factor η			0.58(1)	

about $\alpha_i \approx 12$ mrad. This is seen as a phase shift of the Kiessig fringes in reflectivity curves when the specular reflectivity ridge overlaps with off-specular diffraction bands. Theoretical models for the reflectivity fit cannot describe this effect and reliable results can be obtained only when data in the region $\alpha_i \lesssim 12$ mrad are used in the fit. The reduction of the fitting range may, however, substantially affect the reliability of the resulting fitting parameters. In particular, when cutting off data in the tail of the reflectivity curve one looses information on the low frequency modulation due to the cap layer and on the Debye-Waller factor describing interface and surface roughness. This information was partially recovered via the experiment with the sample rotated by 90° about the normal to its surface.

Small splitting effects across the specular line ridge can be seen in the experimental maps of Fig. 9(b). They are most likely experimental artifacts due to the binning procedure of electronic channels in our PSD. To clarify these splitting effects, we have carried out additional measurements on another stripe array S3, produced with a similar stripe pattern of the same periodicity but with a nominal permalloy thickness of 800 Å. Off-specular scattering maps from the sample S3 with stripes oriented parallel to the scattering plane were collected in fields of 35 and 5200 Oe. The corresponding maps are presented in Ref. [47]. One may notice that the maps from S2 and S3 are quantitatively identical. In particular, the splittings are the same and they are field independent. However, there are two remarkable differences between the maps of samples S2 and S3: first, the Kiessig fringes exhibit an enhanced dip due to the larger thickness of the S3 sample and second, the SF signal is increased at 35 Oe, which is to be expected for a field well below saturation.

2. Parallel orientation of sample S2

Figure 10 reproduces specular and off-specular scattering maps and fits of corresponding specular reflectivities for sample S2 with stripes oriented parallel to the scattering plane as sketched in Fig. 6(b). An external field of 5.2 kOe was applied perpendicular to the stripes during these measurements. Fitting parameters obtained for this case are collected in Table V. In particular, one may notice from the fourth column of this table that the magnetic induction in the ISS is not reduced at all, in contrast to sample S1. Moreover, the stripe surface factor $\eta = 0.58$ should be attributed to the fraction of the surface covered by stripe material. Its complementary to unity factor $1 - \eta = 0.42$ describes, in turn, the fraction of the surface free from material. The latter includes the rim around the pattern and bare Si substrate in the ISS.

3. Discussion of results from sample S2

It is important to note that the off-specular maps for sample S2 are qualitatively different from those obtained for the sample S1. The maps for sample S2 solely display specular reflectivity ridges surrounded, below the critical edge, by low intensity ellipse-shaped halos without Yoneda enhancement effects neither at the critical angles of total reflection from the Si substrate nor at the Py critical angles, despite the latter ones well recognizable in the specular reflectivity curves. Such halos, which asymmetrically border the NSF specular ridges in region below the critical edge and with intensity proportional to the specularly reflected beam, are attributed to parasitic instrumental effect of scattering of the 4.41-Å neutron beam on polycrystalline grains of the bulk 7-mm-thick front aluminium window of the ^{3}He PSD detector. This scattering becomes visible whenever an intense neutron beam, either direct or specularly reflected, hits the detector, and is not related to off-specular scattering from the sample.

For the sample S2 one can conclude that, in contrast to sample S1, the intensity maps do not show any detectable off-specular diffuse scattering caused by irregular magnetic induction between the stripes. This assumes that the rather strong interstripe induction $B_{\|}(z, y)$ is independent of the x coordinate and quite homogeneously distributed with no appreciable random gradients in the x direction along stripes and the incident beam. Field gradients in two orthogonal z and y directions cannot cause off-specular scattering in this sample orientation. Hence the absence of off-specular diffuse scattering means that the system is translation invariant with respect to its shift along the stripes (x axis) for a distance smaller than, or comparable with the long axis of the coherence ellipsoid. This is possible if the edge roughness and, hence, the interstripe field inhomogeneities are both absent, or, alternatively, the edge roughness correlation length in x direction is larger than the coherence length l_x^{coh}. In the latter case the edge roughness may rather be called "edge waviness." The waviness should lead to fluctuations of interstripe distance and affect the lateral Bragg intensity and width in the experimental configuration with stripes oriented perpendicular to the scattering plane. However, such effects of peak broadening or intensity reduction has not been detected and Bragg bands in the maps in Fig. 9 were simulated for the nominal lateral structure with smooth stripe edges and, consequently, homogeneous interstripe magnetic induction.

VI. SUMMARY AND CONCLUSIONS

Edge roughness in ferromagnetic stripe patterns is an important parameter that has a large impact on magnetic domain distributions, domain pinning, and domain propagation. Furthermore, edge roughness is responsible for interaction of magnetic stripes in the direction normal to their long axis. Because of this it is of considerable interest to characterize edge roughness from a structural point of view and even more so from a magnetic perspective. In this contribution, we have shown that using polarized neutron scattering a detailed analysis of the edge roughness is possible. This is not so much due to the structural disturbances that edge roughness invokes, but more due to an inhomogeneous flux distribution that originates from the notches and bulges at the edge of magnetic stripes. When magnetized in the direction perpendicular to the stripe long axis, the magnetic field lines are demanded to exit normal to the surface of these irregularities. This leads to an inhomogeneous magnetic flux distribution in the empty space between stripes. The inhomogeneous flux distribution, in turn, gives rise to pronounced off-specular diffuse magnetic scattering. Therefore quantitative analysis of the off-specular scattering, carried out within the framework of distorted wave Born approximation, in addition to the specular polarized neutron reflectivity provides a bulk of detailed information

on edge roughness in micro- to nanosized laterally patterned arrays inaccessible otherwise.

In this contribution, we have compared the specular reflectivity, the Bragg- and the diffuse off-specular magnetic scattering from two stripe arrays, one with edge roughness and the other one with smooth but wavy edges. Analysis of polarized neutron reflectivity and off-specular diffuse scattering shows that the magnetic induction in the interspatial region between the stripes is reduced by 77.5% [2] in the sample with rough edges, but not reduced at all in the sample with smooth edges. The methods described and discussed here can also be applied to any other lateral magnetic arrays, such as spin ice patterns or skyrmion lattices.

ACKNOWLEDGMENTS

We gratefully acknowledge financial support by the BMBF (Grant No. 05KN7PC1) and by the Institute Laue-Langevin for beamtime. We wish to thank K. Zhernenkov and A. Devishvili for their help during the PNR experiments. Furthermore we would like to thank A. Ludwig and C. Bock for technical support of the sample preparation.

APPENDIX A

Let us consider the effect of a small misalignment of the in-plane tilt angle χ between stripes and longest axes of coherence ellipsoids for the sample S1 in perpendicular geometry shown in Fig. 6(b). In this case, the coherence ellipsoids are mostly displayed either within stripes, or in between of stripes only if $\chi \ll \chi_{\min}$, where $\sin\chi_{\min} \sim w/l_x^{\rm coh} \approx 0.6^\circ$, assuming that $l_x^{\rm coh} \sim 100\,\mu$m and $w = 1.1\,\mu$m. At the same time a small percentage of ellipsoids are partially cover the stripes and the interstripe spacen (ISS). Mean SLD averaged over such ellipsoids is reduced, while their effective width is increased proportionally to the tilt angle. In the limiting case $\chi_{\min} \leqslant \chi \leqslant \chi_{\max}$, where $\sin\chi_{\max} \sim (d-w)/l_x^{\rm coh} \approx 1.8^\circ$, some of the ellipsoids are still displayed between stripes, while others unavoidably cross at least one of stripe boundaries. This should lead to a significant decrease of mean SLD, and can not explain SLD reduction of only 10% observed for the sample S1. Summarizing, the direct study of microstripe edge roughness with PNR requires a control of the tilt angle χ with accuracy better than 0.1°.

APPENDIX B

Fit of specular reflectivities collected from the sample S1 with stripes oriented parallel to the scattering plane was performed using two parameters $\langle\cos\Delta\gamma_{s,i}\rangle_{\rm coh}$ and $\langle\cos\overline{\gamma}_{s,i}\rangle_{\rm inc}$ describing the induction distribution within and between the stripes. The need for these two fit parameters becomes clear considering the two-step surface averaging procedure of the induction fluctuations in detail.

In the first step, the averaging runs over the induction fluctuations correlated over distances within one of the coherence ellipsoids, while in the second step the averaging runs

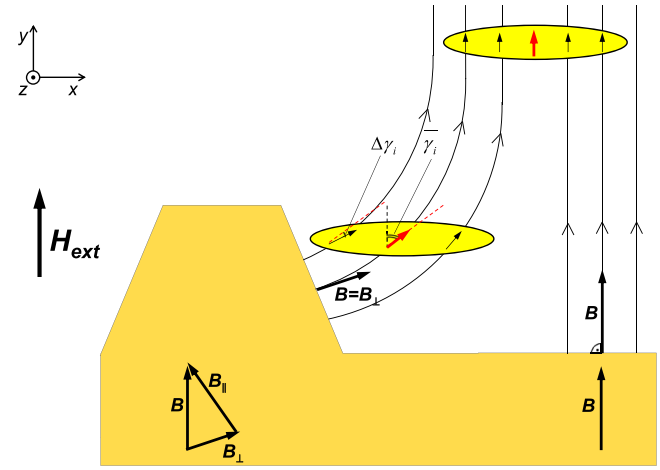

FIG. 11. Surface averaging in PNR. Yellow ellipses represent lateral projections of coherence ellipsoids. Thin black arrows denote vectors of local magnetic induction within ellipsoids, while thick red arrows denote mean magnetization induction vectors $\overline{\boldsymbol{B}}_{s,i}$ averaged over coherence area and tilted by the angle $\overline{\gamma}_{s,i}$ to the external field direction.

over different coherent ellipsoids covering the sample surface exposed by the incident neutron beam. Therefore, as shown in Fig. 11, the tilt angles $\gamma_{s,i}$ between local induction and external field are decomposed into the sum: $\gamma_{s,i} = \overline{\gamma}_{s,i} + \Delta\gamma_{s,i}$, where $\overline{\gamma}_{s,i}$ are the mean values of the tilt angle averaged over each of coherent ellipsoids and may vary over large distances. The angles $\Delta\gamma_{s,i}$, in turn, corresponds to short-distance fluctuations $\Delta\boldsymbol{B}_{s,i} = \boldsymbol{B}_{s,i} - \overline{\boldsymbol{B}}_{s,i}$ of the magnetic induction inside the individual coherence ellipsoids. These fluctuations are counted with respect to mean magnetic induction $\overline{\boldsymbol{B}}_{s,i}$ which directions are constrained by the conditions $\langle\sin\Delta\gamma_{s,i}\rangle_{\rm coh} = 0$.

In accordance with these constrains the reduced mean values of SLD are written as follows:

$$Nb_{s,i}^{\pm} = Nb_n^{s,i} \pm \langle\cos\Delta\gamma_{s,i}\rangle_{\rm coh} Nb_m^{s,i}, \tag{B1}$$

where the nuclear SLD in between the stripes is $Nb_n^i = 0$, while the magnetic SLDs $Nb_m^{s,i}$ are expressed via the respective inductions in accordance with Eq. (5).

The mean directions of the induction vectors $\overline{\boldsymbol{B}}_{s,i} = \langle\boldsymbol{B}_{s,i}\rangle_{\rm coh}$ averaged over the coherence ellipsoid may not be parallel to the external field, but tilted by the angle $\overline{\gamma}_{s,i}$ different for different ellipsoids and hence varying within the surface plane over large distances. For example, for the bottom-left ellipsoid shown in Fig. 11 the mean induction vector is tilted at the angle $\overline{\gamma}_i \approx 70^\circ$, whereas for the upper-right ellipsoid far away from the notch $\overline{\gamma}_i = 0$. Correspondingly, the model used in the fit includes both types of averaging: the one accomplished over the coherence ellipsoids and described by the parameter $\langle\cos\Delta\gamma_i\rangle_{\rm coh}$, and the other one running over the whole surface and described by the parameter $\langle\cos\overline{\gamma}_i\rangle_{\rm inc}$ given for sample S1 in the Table III as a result of the fit in accordance with Eq. (4). In that equation, the reflectivities $R^{\pm}$ are substituted by their mean values

$$\overline{R}^{\pm} = \eta\overline{R}_s^{\pm} + (1-\eta)\overline{R}_i^{\pm}, \tag{B2}$$

[2]Total reduction factor of interstripe magnetic induction $1 - \langle\cos\Delta\gamma\rangle_{\rm coh}\langle\cos\overline{\gamma}\rangle_{\rm inc} = 1 - 0.75\times 0.3 = 77.5\%$.

incoherently averaged over tilt angles $\overline{\gamma}_s$ and $\overline{\gamma}_i$ within and between stripes, respectively, for SLDs in Eq. (B1). After such averaging,

$$\overline{R}^{\pm}_{s,i} = \tfrac{1}{2}\{[R^{+}_{s,i} + R^{-}_{s,i}] \pm P_i\langle\cos\overline{\gamma}_{s,i}\rangle_{\rm inc}[R^{+}_{s,i} - R^{-}_{s,1}]\}, \quad \text{(B3)}$$

where P_i is the neutron incident beam polarization.

APPENDIX C

The theoretical model used for simulating the OSS maps is based on a set of structural parameters characterizing the layer stack including layer SLDs and thicknesses, interface roughnesses, mean interstripe induction, surface factor and mean value $\langle\cos\overline{\gamma}_s\rangle_{\rm inc}$, which were fixed in simulations at their values deduced from the fit of specular reflectivities. These parameters describe not only reflectivities in Fig. 8(a), but also distortions of neutron wave field in the mean potential due to optical effects: transmission into the range of potential, reflection from its borders and birefringence [50,51] effects caused by the Zeeman splitting of neutron spin states e.g. in the ISS. In there, distorted waves are scattered in off-specular directions if local induction deviations $\Delta\boldsymbol{B}_i = \Delta\boldsymbol{B}_i(x, y)$ are correlated over distances smaller than the coherence volume. The vector $\Delta\boldsymbol{B}_i$ can be decomposed over its orthogonal projections $\Delta B^{\perp}_i = B_i \sin\Delta\gamma_i$ and $\Delta B^{\parallel}_i = B_i(\cos\Delta\gamma_i - \langle\cos\Delta\gamma_i\rangle_{\rm coh})$, so that their mean values $\langle\Delta B^{\parallel}_i\rangle_{\rm coh} = \langle\Delta B^{\perp}_i\rangle_{\rm coh} = 0$. At the same time, the correlation functions $G^{\perp,\parallel}_i(x - x', y - y') = \langle\Delta B^{\perp,\parallel}_i(x, y)\cdot\Delta B^{\perp,\parallel}_i(x', y')\rangle_{\rm coh} \neq 0$ and their Fourier transforms averaged over different coherence ellipsoids covering the whole sample surface determine the magnetic cross section of OSS in DWBA. The incoherent averaging procedure is substantially simplified due to the strong anisotropy of coherence ellipsoids.

As discussed above and illustrated in Fig. 6(b), the coherence length $l^{\rm coh}_y$ in the direction normal to stripe edges is much shorter than the coherence length $l^{\rm coh}_x$ parallel to the stripes. On the other hand, as seen from Fig. 8(d), the OSS petal-like diffuse magnetic intensity distributions are well separated from specular reflection indicating that the correlation length of induction fluctuations ξ_x, which is scaled with the correlation length of edge roughness, is sufficiently large, but still smaller than $l^{\rm coh}_x$. Therefore one can assume that $l^{\rm coh}_y \ll \xi_x \leqslant l^{\rm coh}_x$ and neglect the difference $y - y' \approx 0$ between arguments y and y' in the correlation function above. As a result, the correlators of induction fluctuations are determined by 1D, but not by 2D Fourier transforms:

$$G^{\perp,\parallel}_i(q_x) = \int dx e^{-iq_x x}\overline{G}^{\perp,\parallel}_i(x), \quad \text{(C1)}$$

where $\overline{G}^{\perp,\parallel}_i(x)$ denote correlation functions integrated over coordinate $y' = y$ over the ISS.

In order to bring the number of extra parameters sufficient to describe our data on OSS to a minimum, we further assume that $\overline{G}^{\perp,\parallel}(x) = \overline{G}^{\perp,\parallel}(0)e^{-|x|/\xi_x}$, where $\overline{G}^{\perp,\parallel}(0)$ are the mean square amplitudes of induction fluctuations and $\overline{G}^{\perp}(0) = B^2\langle\sin^2\Delta\gamma_i\rangle_{\rm coh}$, whereas $\overline{G}^{\parallel}(0) = B^2[\langle\cos^2\Delta\gamma_i\rangle_{\rm coh} - \langle\cos\Delta\gamma_i\rangle^2_{\rm coh}] \geqslant 0$. The latter two parameters are not independent, because of the equation $\langle\cos^2\Delta\gamma_i\rangle_{\rm coh} = 1 - \langle\sin^2\Delta\gamma_i\rangle_{\rm coh}$, while the value of $\langle\cos\Delta\gamma_i\rangle_{\rm coh}$ was already determined from the fit of specular reflectivity. Hence, varying two remaining free parameters ξ_x and $\langle\sin^2\Delta\gamma_i\rangle_{\rm coh}$ the best agreement between simulated intensities of OSS and experimentally measured off-specular maps was achieved at the values of the correlation length $\xi \approx 3.5$ μm and the mean square $\langle\sin^2\Delta\gamma_i\rangle_{\rm coh} \approx 0.44$. This value corresponds to $\langle\cos^2\Delta\gamma_i\rangle_{\rm coh} \approx 0.56$, which is close to the square $\langle\cos\Delta\gamma_i\rangle^2_{\rm coh}$, so that the dispersion $\langle\cos^2\Delta\gamma_i\rangle_{\rm coh} - \langle\cos\Delta\gamma_i\rangle^2_{\rm coh} \approx 0$ and the OSS is mainly due to correlations of induction components perpendicular to its mean direction determined by the angle $\overline{\gamma}_i$.

The other feature related to OSS not yet considered are some flux gradients along the surface normal forming a flattened barrel-like distribution over the z axes. A statistical smearing of the interstripe induction layer was imitated by an error function with a width $W_i \approx 60$Å allowing for further improvement of agreement between experimental and simulated maps in Fig. 8(d). In particular, such smearing of magnetic potential in z direction limits the extension of OSS along lines $\alpha_i \approx \alpha_c$ and $\alpha_f \approx \alpha_c$ suppressing long Lorentzian tails in the maps that correspond to an exponential decay of the correlation function.

[1] A. Bisig, M. Stärk, M. Mawass, C. Moutafis, J. Rhensius, J. Heidler, F. Büttner, M. Noske, M. Weigand, S. Eisebitt, T. Tyliszczak, B. V. Waeyenberge, H. Stoll, G. Schütz, and M. Kläui, Nat. Commun. **4**, 2328 (2013).

[2] O. Petracic, P. Szary, H. Zabel, D. Goerlitz, and K. Nielsch, Superlattices Microstruct. **46**, 728 (2009).

[3] B. Hausmanns, T. P. Krome, G. Dumpich, E. F. Wassermann, D. Hinzke, U. Nowak, and K. D. Usadel, J. Magn. Magn. Mater. **240**, 297 (2002).

[4] W. C. Uhlig, and J. Shi, Appl. Phys. Lett. **84**, 759 (2004).

[5] Y. Kasatani, A. Yamaguchi, H. Yamamoto, and H. Miyajima, Phys. Rev. B **81**, 224425 (2010).

[6] G. S. D. Beach, C. Nistor, C. Knutson, M. Tsoi, and J. L. Erskine, Nat. Mater. **4**, 741 (2005).

[7] T. Ono, H. Miyajima, K. Shigeto, K. Mibu, N. Hosoito, and T. Shinjo, Science **284**, 468 (1999).

[8] D. Atkinson, D. A. Allwood, G. Xiong, M. D. Cooke, C. C. Faulkner, and R. P. Cowburn, Nat. Mater. **2**, 85 (2003).

[9] Y. Yokoyama, Y. Suzuki, S. Yuasa, K. Ando, K. Shigeto, T. Shinjo, P. Gogol, J. Miltat, A. Thiaville, T. Ono, and T. Kawagoe, J. Appl. Phys. **87**, 5618 (2000).

[10] H. Du, R. Che, L. Kong, X. Zhao, C. Jin, C. Wang, J. Yang, W. Ning, R. Li, C. Jin, X. Chen, J. Zang, Y. Zhang, and M. Tian, Nat. Commun. **6**, 8504 (2015).

[11] Z. Hou, Q. Zhang, G. Xu, C. Gong, B. Ding, Y. Wang, H. Li, E. Liu, F. Xu, H. Zhang, Y. Yao, G. Wu, X. Zhang, and W. Wang, Nano Lett. **18**, 1274 (2018).

[12] J. Chi-Ming, and D. Hai-Feng, Chin. Phys. B **24**, 128501 (2015).

[13] C. Jin, Z.-A. Li, A. Kovacs, J. Caron, F. Zheng, F. N. Rybakov, N. S. Kiselev, H. Du, S. Bluegel, M. Tian, Y. Zhang, M. Farle, and R. E. Dunin-Borkowski, Nat. Commun. **8**, 15569 (2017).

[14] X. Zhang, J. Xia, G. Zhao, H. Fangohr, M. Ezawa, and Y. Zhou, Racetrack-type Applications of Magnetic Skyrmions, in *Skyrmions Topological Structures, Properties and Applications*, edited by J. P. Liu, Z. Zhang, and G. Zhao (CRC, Taylor & Francis Group, Boca Raton, 2016).

[15] C. Hanneken, A. Kubetzka, K. von Bergmann, and R. Wiesendanger, New J. Phys. **18**, 055009 (2016).

[16] K. Everschor-Sitte, J. Masell, R. M. Reeve, and M. Kläui, J. Appl. Phys. **124**, 240901 (2018).

[17] A. Singh, J. C. T. Lee, K. E. Avila, Y. Chen, S. A. Montoya, E. E. Fullerton, P. Fischer, K. A. Dahmen, S. D. Kevan, M. K. Sanyal, and S. Roy, Nat. Commun. **10**, 1988 (2019).

[18] K. Gross, P. Szary, O. Petracic, F. Brüssing, K. Westerholt, and H. Zabel, Phys. Rev. B **84**, 054456 (2011).

[19] J. McCord, T. Schmitte, R. Schafer, H. Zabel, and L. Schultz, IEEE Trans. Magn. **39**, 2687 (2003).

[20] E. Seynaeve, G. Rens, A. V. Volodin, K. Temst, C. Van Haesendonck, and Y. Bruynseraede, J. Appl. Phys. **89**, 531 (2001).

[21] B. Leven, and G. Dumpich, Phys. Rev. B **71**, 064411 (2005).

[22] S. S. P. Parkin, M. Hayashi, and L. Thomas, Science **320**, 190 (2008).

[23] R. Sbiaa and S. N. Piramanayagam, Appl. Phys. A **114**, 1347 (2014).

[24] D. A. Allwood, G. Xiong, C. C. Faulkner, D. Atkinson, D. Petit, and R. P. Cowburn, Science **309**, 1688 (2005).

[25] D. Atkinson, C. C. Faulkner, D. A. Allwood, and R. P. Cowburn, Domain-Wall Dynamicsin Magnetic Logic Devices, in *Spin Dynamics in Confined Magnetic Structures III*, edited by B. Hillebrands and A. Thiaville, Topics in Applied Physics Vol. 101 (Springer, Berlin, Heidelberg, 2006).

[26] M. T. Bryan, D. Atkinson, and R. P. Cowburn, Appl. Phys. Lett. **85**, 3510 (2004).

[27] M. T. Bryan, D. Atkinson, and R. P. Cowburn, J. Phys.: Conf. Ser. **17**, 40 (2005).

[28] M. Kläui, H. Ehrke, U. Rüdiger, T. Kasama, R. E. Dunin-Borkowski, D. Backes, L. J. Heyderman, C. A. F. Vaz, J. A. C. Bland, G. Faini, E. Cambril, and W. Wernsdorfer, Appl. Phys. Lett. **87**, 102509 (2005).

[29] C. C. Faulkner, M. D. Cooke, D. A. Allwood, D. Petit, D. Atkinson, and R. P. Cowburn, J. Appl. Phys. **95**, 6717 (2004).

[30] D. Petit, A.-V. Jausovec, D. Read, and R. P. Cowburn, J. Appl. Phys. **103**, 114307 (2008).

[31] T. W. Chiang, L. J. Chang, C. Yu, S. Y. Huang, D. C. Chen, Y. D. Yao, and S. F. Lee, Appl. Phys. Lett. **97**, 022109 (2010).

[32] J. G. Deak and R. H. Koch, J. Magn. Magn. Mater. **213**, 25 (2000).

[33] H. Zabel, K. Theis-Bröhl, M. Wolff, and B. P. Toperverg, IEEE Trans. Magn. **44**, 1928 (2008).

[34] K. Temst, E. Popova, M. J. Van Bael, H. Loosvelt, J. Swerts, D. Buntinx, Y. Bruynseraede, C. Van Haesendonck, H. Fritzsche, M. Gierlings, L. H. A. Leunissen, and R. Jonckheere, J. Appl. Phys. **97**, 10K117 (2005).

[35] K. Temst, M. J. Van Bael, J. Swerts, H. Loosvelt, E. Popova, D. Buntinx, J. Bekaert, C. Van Haesendonck, Y. Bruynseraede, R. Jonckheere, and H. Fritzsche, Superlattices Microstruct. **34**, 87 (2003).

[36] K. Temst, E. Girgis, R. D. Portugal, H. Loosvelt, E. Popova, M. J. Van Bael, C. Van Haesendonck, H. Fritzsche, M. Gierlings, L. H. A. Leunissen, and R. Jonckheere, Eur. Phys. J. B **45**, 261 (2005).

[37] C. Hamann, J. McCord, L. Schultz, B. P. Toperverg, K. Theis-Bröhl, M. Wolff, R. Kaltofen, and I. Mönch, Phys. Rev. B **81**, 024420 (2010).

[38] K. Theis-Bröhl, B. P. Toperverg, V. Leiner, A. Westphalen, H. Zabel, J. McCord, K. Rott, and H. Brückl, Phys. Rev. B **71**, 020403(R) (2005).

[39] K. Theis-Bröhl, H. Zabel, J. McCord, and B. P. Toperverg, Physica B **356**, 14 (2005).

[40] K. Theis-Bröhl, M. Wolff, A. Westphalen, H. Zabel, J. McCord, V. Höink, J. Schmalhorst, G. Reiss, T. Weis, D. Engel, A. Ehresmann, U. Rücker, and B. P. Toperverg, Phys. Rev. B **73**, 174408 (2006).

[41] K. Theis-Bröhl, A. Westphalen, H. Zabel, U. Rücker, J. McCord, V. Höink, J. Schmalhorst, G. Reiss, T. Weis, D. Engel, A. Ehresmann, and B. P. Toperverg, New J. Phys. **10**, 093021 (2008).

[42] B. P. Toperverg and H. Zabel, in *Neutron Scattering in Nanomagnetism*, edited by F. Fernandez-Alonso and D. L. Price, Experimental Methods in the Physical Sciences Vol. 48 (Elsevier, Amsterdam, 2016), pp. 339–434.

[43] B. P. Toperverg, Phys. Met. Metallogr. **116**, 1337 (2015).

[44] H. Zabel, K. Theis-Bröhl, and B. P. Toperverg, *Polarized Neutron Reflectivity and Scattering from Magnetic Nanostructures and Spintronic Materials*, edited by H. Kronmüller and S. Parkin, Handbook of Magnetism and Advanced Magnetic Materials Vol. 3 (Wiley, New York, 2007).

[45] A. Devishvili, K. Zhernenkov, A. J. C. Dennison, B. P. Toperverg, M. Wolff, B. Hjorvarsson, and H. Zabel, Rev. Sci. Instrum. **84**, 025112 (2013).

[46] V. Syromyatnikov, A. Schebetov, D. Lott, A. Bulkin, N. Pleshanov, and V. Pusenkov, Nucl. Instrum. Methods **634**, S126 (2011).

[47] See Supplemental Material at http://link.aps.org/supplemental/10.1103/PhysRevB.101.224404 for calculated partial reflectivities $R^{\pm}_{s,i}$ (part A), calculated maps assuming zero induction $B_i = 0$ between the stripes (part B), and off-specular scattering maps from the sample S3 (part C).

[48] Y. Yoneda, Phys. Rev. **131**, 2010 (1963).

[49] N. F. Mott and H. S. W. Massey, *The Theory of Atomic Collisions* (Clarendon,Oxford, 1965).

[50] R. Günther, W. Donner, B. P. Toperverg, and H. Dosch, Phys. Rev. Lett. **81**, 116 (1998).

[51] B. P. Toperverg, A. Rühm, W. Donner, and H. Dosch, Physica B **267-268**, 198 (1999).